

CrossMark
click for updatesCite this: *J. Mater. Chem. A*, 2016, 4,
13307

2D hydrated layered Ni(OH)₂ structure with hollow TiO₂ nanocomposite directed chromogenic and catalysis capabilities†

Wei Li Ong,^a Serene Wen Ling Ng,^a Chun Zhang,^{bc} Minghui Hong^a
and Ghim Wei Ho^{*abd}

Two-dimensional (2D) hydrated layered structures have emerged as a fascinating new class of materials for diversified surface mediated redox reactions. Here, a solution-processable 2D hydrated layered structure, Ni(OH)₂ nanosheets with hollow TiO₂ nanosphere composite has been designed to realize complementary electrochemical and catalysis reactions. The inherent 2D anisotropic lamellar hydrated framework of Ni(OH)₂ contains interstitial spaces to promote efficient and reversible insertion/extraction of electrolyte ions without compromising its structural integrity. This translates to a fast switching speed and high stability valence change of metal ions that actively tunes the optical transmittance. Additionally, the Ni(OH)₂ nanosheets synergistically play a co-catalyst role to enhance the photocatalytic degradation reactivity of TiO₂ nanospheres. Correspondingly, the TiO₂ nanospheres are composed of a porous thin shell that provides abundant active sites, distinct cavity diameter with enhanced light harvesting and improved reactant accessibility with a porous framework. Collectively, the nanocomposite is devised to exemplify a monolithically integrated multiple functionalities material system that unprecedentedly delivers photocatalytic degradation coupled electrochromism for environmental and energy conservations.

Received 20th May 2016
Accepted 1st August 2016

DOI: 10.1039/c6ta04199j

www.rsc.org/MaterialsA

Introduction

Recently, rapidly emerging two-dimensional (2D) structured nanomaterials have been intensely investigated due to their unconventional properties and vast promising technological applications. Other than the well-known graphene,¹ 2D nanosheets of various materials including layered double hydroxides,^{2,3} transition-metal chalcogenides,⁴ metal oxides⁵ and hydroxides have also caught up with the worldwide research interest. Essentially, such anisotropic 2D nanomaterials largely made up of surfaces with molecular-scale thickness possess strong quantum confinement of electrons in lateral dimensions and a high surface to volume ratio. Furthermore, ultrathin 2D nanostructures bestow short diffusion path distance, numerous active sites, extensive interfacial contact area, high electronic conductivity, and improved structural stability.⁶ With the host

of attributes, a 2D nanostructured material is an ideal and promising candidate for comprehensive surface mediated reactions ranging from sensing, catalysis, chromism to energy production, conversion and storage processes.

2D nanomaterials, in particular the layered structures, are highly sought after since they possess unique strong lateral chemical bonding in planes contrasting with the weak van der Waals interaction between planes. The lamellar host framework consists of adequate interstitial spaces that facilitate high diffusion and insertion–extraction of guest species. Furthermore, such a lamellar structure is expected to buffer volume changes, or minimize strain effect hence improving long-term cycling stability.⁷ Additionally, water/hydroxyl/oxy-hydroxyl containing 2D layered structures are gaining interest owing to their favorable effects in electrochemistry and electrocatalysis. It has been shown that water molecules present in the hydrated layered structures enhance the diffusion coefficient and ionic conductivity.⁸ Also, the existence of hydroxyl groups shows improved ion diffusion at the film electrolyte interface.⁹

However, the common methodologies for synthesizing 2D layered nanostructured materials including exfoliation of bulk crystals and vapor phase deposition pose various challenges.^{10–13} The former method results in low throughput, uncontrollable geometric features, *i.e.* shape, size and thickness, while the latter produces low yield along with high temperature, stringent vacuum conditions and specific noble

^aDepartment of Electrical and Computer Engineering, National University of Singapore, 4 Engineering Drive 3, Singapore 117583. E-mail: elehgw@nus.edu.sg

^bEngineering Science Programme, National University of Singapore, 9 Engineering Drive 1, Singapore 117575

^cDepartment of Physics, National University of Singapore, Singapore

^dInstitute of Materials Research and Engineering, A*STAR (Agency for Science, Technology and Research), 3 Research Link, Singapore 117602

† Electronic supplementary information (ESI) available. See DOI: 10.1039/c6ta04199j

metal catalyzed substrate requirements. At times, extra and harsh processing steps may be needed to separate the single-layer sheets from the substrate depending on the end applications. All these challenges hinder the large-scale and cost-effective production of 2D layered nanomaterials.

Herein, we report a solution processable 2D hydrated layered structure, Ni(OH)₂ nanosheets with hollow TiO₂ nanosphere cores that leverage on the synergistic structural-composition design for desired surface mediated electrochromism coupled catalysis reactions. The hydrated layered structure Ni(OH)₂ with its intrinsic lamellar framework promotes reversible intercalation or deintercalation of ions. This is accompanied by fast switching speed and high stability valence change of metal ions that actively and reversibly tune the optical transmittance. In conjunction, Ni(OH)₂ serves as a co-catalyst to minimize photogenerated electron-hole pair recombination, *i.e.* to enhance the efficiency of charge separation of TiO₂, thereby improving its photocatalytic degradation activity. In regard to TiO₂ nanospheres, a thin shell with reduced charge carrier diffusion length, distinct cavity diameter with enhanced light harvesting and improved reactant accessibility with its porous framework is constructed. Moreover, the porous thin shell imparts high specific surface area with a large number of active sites for increased rates of reaction. This synthesis effort highlights a monolithically integrated multiple functionalities material system that plays a pivotal role in photocatalytic environmental and chromogenic energy conservations. The electrochromism coupled photodegradation functions warrant greater thermal comfort and a cleaner indoor environment that are likely to meet the future emerging building requirements.

Experimental methods

Synthesis of SiO₂ spheres

24 ml of ammonia was added into 81 ml of ethanol and stirred at 600 rpm for 30 s, following which the stirring speed was increased to 800 rpm. 4.2 ml of tetraethyl orthosilicate (TEOS, Sigma Aldrich) was then added slowly into the mixture and left to stir at 800 rpm for 1 h. The product was centrifuged and washed 3 times with deionized (DI) water followed by one time with ethanol. The product was eventually dried at 55 °C and collected for further use.

Synthesis of SiO₂@TiO₂ spheres

0.1 g of SiO₂ spheres was dispersed in 2 ml of ethanol by ultrasonication for 5 min. 0.235 ml of titanium *n*-butoxide (TBT, Sigma Aldrich) was then added into the solution of SiO₂ spheres. The mixture was stirred at 350 rpm for 20 min and named solution I. Solution II was prepared by dissolving 0.3 g of polyvinylpyrrolidone (PVP, Sigma Aldrich) in 20 ml of ethanol and 1 ml of DI water. This solution was then added to solution I and left to stir at 300 rpm for 1 h. The resultant product was centrifuged and washed twice with ethanol, followed by drying at 55 °C. The dried product was then calcined at 450 °C for 2 h, with a ramping rate of 2 °C min⁻¹.

Synthesis of TiO₂@Ni(OH)₂ hierarchical hollow spheres

The SiO₂@TiO₂ spheres were dispersed in 30 ml of DI water by ultrasonication, followed by the addition of nickel nitrate (Ni(NO₃)₂, Acros Organics) and hexamethyltetramine (HMT, Sigma Aldrich). The mixture was then transferred to a Teflon-lined autoclave and heated at 100 °C for 4 h. The product was centrifuged and washed with DI water several times before drying at 80 °C for 2 h.

Materials characterization

The morphology of the TiO₂@Ni(OH)₂ hierarchical hollow spheres was characterized with a scanning electron microscope (SEM, JEOL FEG JSM 7001F) operated at 15 kV. The elements present in the nanostructures were analyzed using energy-dispersive X-ray spectroscopy (EDX, Oxford Instruments) and also scanning transmission electron microscopy (STEM, JEOL 2100 TEM). The crystalline structures of the TiO₂@Ni(OH)₂ composite were analyzed using X-ray diffraction (XRD, D5005 Bruker X-ray diffractometer with graphite-monochromated Cu K α radiation at $\lambda = 1.541 \text{ \AA}$) and transmission electron microscopy (TEM, JEOL 2100 TEM). Brunauer-Emmett-Teller (BET, Quantachrome Nova 1200) measurements were conducted with nitrogen (N₂) as the adsorbate at liquid nitrogen temperature. Absorption and transmission spectra of the samples were measured with a UV-VIS-NIR spectrophotometer (UV-VIS, Shimadzu UV-3600). Fourier transform infrared (FT-IR) spectra of the products were recorded on a Shimadzu IRPrestige-21 FT-IR spectrophotometer. Thermal imaging was carried out using an FLIR E50 thermal camera. The concentrations of volatile organic compounds (VOCs) were measured by gas chromatography mass spectrometry (Shimadzu GCMS-QP2010 Ultra). The real-time transmittance measurement was carried out with a spectrophotometer (Ocean Optics Maya2000 Pro) and a 550 nm light emitting diode (LED) was used as the light source. The cyclic voltammetry (CV) measurement was carried out with a CHI660e electrochemical workstation.

Electrochromic measurements

The TiO₂@Ni(OH)₂ composite was dispersed in ethanol and spincoated onto fluorine-doped tin oxide (FTO) glass. The coated FTO glass was then dried at 100 °C for 1 h. The sample (working electrode) was placed in 1 M NaOH electrolyte solution and a Pt foil was used as the counter electrode. A forward voltage bias was applied to induce a color change in the TiO₂@Ni(OH)₂ coating and a reverse bias was applied to bleach the electrochromic layer. The absorption and transmittance spectra of the samples were measured with a UV-VIS-NIR spectrophotometer.

Cyclic voltammetry (CV) measurement

The CV measurement was carried out with a CHI660e electrochemical workstation with an Ag/AgCl reference electrode, Pt counter electrode and Ni(OH)₂ or TiO₂@Ni(OH)₂ coated on FTO glass as the working electrode.

Photocatalytic oxidation of VOCs

2 mg of the powdered photocatalyst was coated on a 1.5×2.5 cm glass substrate which was then placed in a quartz vial reactor. The reactor was filled with the VOC vapor with a concentration of 200 ppm and two types of VOCs were tested, namely methanol and formaldehyde. The reactor was then illuminated with a 160 mW light emitting diode (LED) of wavelength 365 nm. 100 μ l gas samples were extracted at regular time intervals using a gas-tight syringe and injected into a GCMS to determine the concentration of VOCs remaining in the reactor.

Results and discussion

The process flow of the $\text{TiO}_2@Ni(\text{OH})_2$ hierarchical composite is illustrated in Fig. 1a. SiO_2 spheres were synthesized according to a modified Stober method,¹⁴ and spheres with a uniform size of ~ 400 nm were obtained (Fig. 1b and c). The spheres were then coated with a thin TiO_2 shell through the hydrolysis of titanium(IV) butoxide (Fig. 1d and e). The TEM image in Fig. 1e shows the core-shell structure where the SiO_2 core is encapsulated by a 50 nm thick TiO_2 shell. $Ni(\text{OH})_2$ nanosheets were then grown on the $\text{SiO}_2@TiO_2$ core-shell spheres by a hydrothermal method. During the synthesis process of $Ni(\text{OH})_2$ nanosheets, HMT decomposes to OH^- ions in the growth solution which is responsible for the formation of $Ni(\text{OH})_2$ and the simultaneous etching of the SiO_2 core. This dual process results in the uniform growth of thin $Ni(\text{OH})_2$ nanosheets on TiO_2 hollow nanospheres (Fig. 1f and g).

The structural design of nanocomposites such as the surface area, cavity size, pore diameter and architecture is known to directly affect the reactant diffusion and light absorption capabilities which play important roles in surface mediated electrochemical and catalysis reactions. On account of electrochemical and catalytic reactivity kinetically controlled by the ion adsorption-diffusion in the pores, surface areas and pore sizes of the various structures were investigated using BET. The N_2 adsorption-desorption isotherm and the corresponding Barrett-Joyner-Halenda (BJH) pore size distributions (inset) of the $\text{TiO}_2@Ni(\text{OH})_2$ nanocomposite are shown in Fig. 1h while the isotherms of $\text{SiO}_2@TiO_2$ spheres and TiO_2 hollow spheres are appended in Fig. S1.† The isotherms can be categorized as type IV which signifies typical mesoporous structures along with hysteresis loops observed at a relative pressure of 0.4 to 0.9. The BET specific surface area obtained from the $\text{SiO}_2@TiO_2$ core-shell spheres is $30.311 \text{ m}^2 \text{ g}^{-1}$ while that of the TiO_2 hollow nanospheres is $71.829 \text{ m}^2 \text{ g}^{-1}$. It is noted that the $\text{TiO}_2@Ni(\text{OH})_2$ hierarchical hollow spheres exhibited the highest surface area of $85.463 \text{ m}^2 \text{ g}^{-1}$ which validates the increase in surface area due to the addition of thin $Ni(\text{OH})_2$ nanosheets that are radially deposited on the mesoporous TiO_2 hollow nanospheres. All the structures possess mesopores with a wide distribution of 3.4–9.6 nm. From the UV-vis absorption spectra presented in Fig. 1i, the $\text{TiO}_2@Ni(\text{OH})_2$ nanocomposite shows distinctly higher light absorption enhancement in the UV and visible regions compared to hollow TiO_2 and $\text{SiO}_2@TiO_2$ core-shell structures. Notably, the as-synthesized $\text{TiO}_2@Ni(\text{OH})_2$

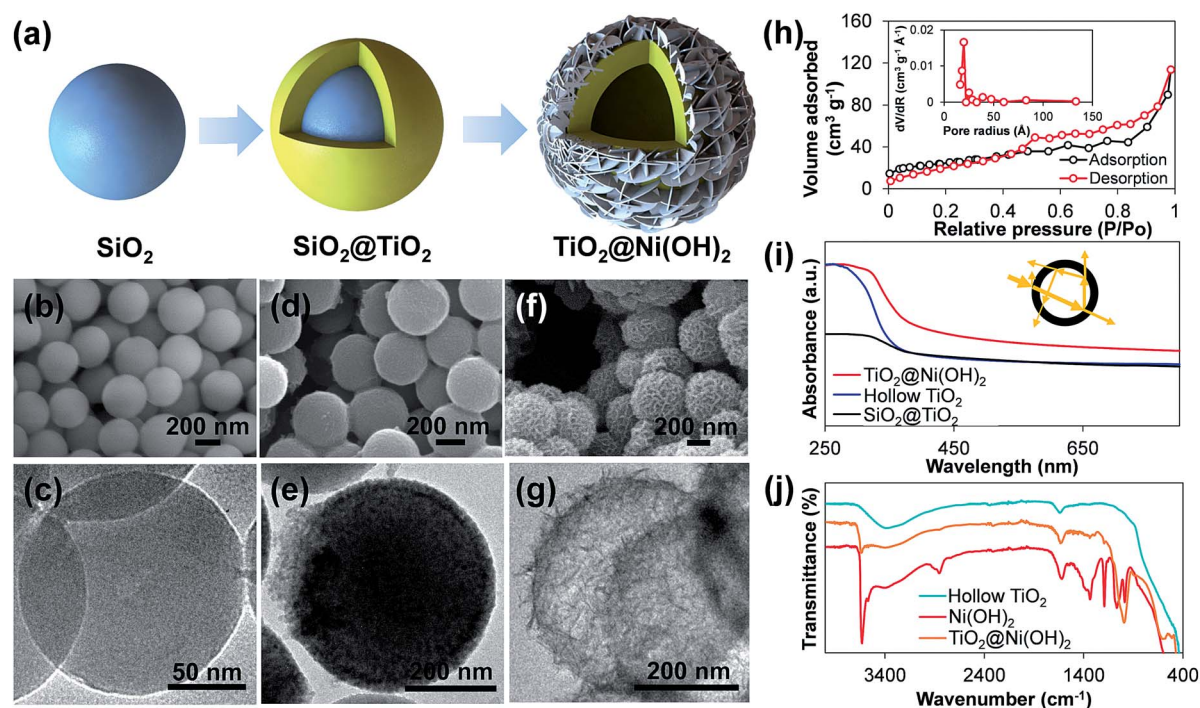


Fig. 1 (a) Schematic diagram showing the formation of $\text{TiO}_2@Ni(\text{OH})_2$ hierarchical hollow spheres. SEM and TEM of (b and c) SiO_2 spheres, (d and e) $\text{SiO}_2@TiO_2$ spheres, and (f and g) $\text{TiO}_2@Ni(\text{OH})_2$ hierarchical hollow spheres. (h) BET of $\text{TiO}_2@Ni(\text{OH})_2$ hierarchical hollow spheres. (i) UV-vis absorption spectra of the various composites. (j) FTIR spectra of TiO_2 hollow nanospheres, $Ni(\text{OH})_2$ nanosheets, and $\text{TiO}_2@Ni(\text{OH})_2$ hierarchical hollow spheres.

possesses a hollow TiO_2 core with a cavity diameter comparable to the UV excitation wavelength (~ 400 nm). It has demonstrated resonance effect in light scattering, and Mie scattering occurs when the cavity diameter of hollow structures is comparable to the incident light wavelength.^{15,16} This leads to effective multiple-scattering within the hollow cavity as schematically represented in Fig. 1i inset. Additionally, the presence of small geometry interparticle voids relative to the wavelength of the incident light brings about Rayleigh scattering.¹⁷ In this case, the interparticle voids are evidently present as mesopores of TiO_2 hollow spheres and $\text{Ni}(\text{OH})_2$ nanosheets as determined by BET shown in Fig. 1h and S1 (ESI[†]). Consequently, the $\text{TiO}_2@/\text{Ni}(\text{OH})_2$ nanocomposite which possesses several built-in critical features, such as high surface area, hollow cavity and mesoporous structures, renders abundant active sites, highly accessible mass diffusion pathways and enhanced light scattering that are collectively beneficial for photo and electrochemical reactivity.

The FTIR spectra of TiO_2 hollow spheres, $\text{Ni}(\text{OH})_2$ nanosheets and $\text{TiO}_2@/\text{Ni}(\text{OH})_2$ are shown in Fig. 1j. The TiO_2 spectrum shows a broad band observed in the range of $400\text{--}900\text{ cm}^{-1}$ due to the characteristic vibrations of the inorganic Ti–O stretch.¹⁸ The transmittance bands observed at 3360 cm^{-1} and 1630 cm^{-1} are ascribed to stretching vibrations of the O–H groups and the bending vibrations of the adsorbed water molecules, respectively. These bands are observed to be higher in the case of $\text{Ni}(\text{OH})_2$ and $\text{TiO}_2@/\text{Ni}(\text{OH})_2$, which may suggest increase in the hydration species content inherently present in hydroxide structures. The $\text{Ni}(\text{OH})_2$ spectrum shows a sharp band at 3630 cm^{-1} associated with the $\nu(\text{OH})$ stretching vibration while the peaks located at *ca.* 630 and 520 cm^{-1} are assigned to the Ni–O–H bending and Ni–O stretching vibrations, respectively. The peak at 1380 cm^{-1} is due to the bending vibration of the residual NO_3^- ions.¹⁹

Fig. 2a shows the low resolution TEM image of the hollow TiO_2 nanospheres made up of well-defined hollow cavities and mesoporous shells. Higher resolution analyses of the hollow core structure at marked regions reveal the presence of highly crystalline TiO_2 nanocrystallites (Fig. 2b). The lattice planes of TiO_2 nanocrystallites are clearly visible at both selected areas with a *d*-spacing of 0.35 nm which can be indexed to the (101) plane of anatase TiO_2 (Fig. 2c and d). Fig. 2e shows the TEM image of the $\text{TiO}_2@/\text{Ni}(\text{OH})_2$ nanocomposite which consists of 2D sheet-like structures radially assembled on the TiO_2 hollow nanospheres. The homogeneous and densely packed nanosheets with hollow TiO_2 nanospheres demonstrate that 3D hierarchical core-shell nanostructured composites have been successfully synthesized. The intrinsic driving force of lamellar nickel hydroxide has enabled 2D anisotropic growth of expansive and thin planar sheets (Fig. 2f and g). The fairly transparent characteristic of the $\text{Ni}(\text{OH})_2$ nanosheets suggests the existence of thin 2D sheet-like structures. The HRTEM image of $\text{Ni}(\text{OH})_2$ in Fig. 2h also shows clear lattice fringes with a lattice spacing of 0.27 nm which corresponds to the (100) plane of $\beta\text{-Ni}(\text{OH})_2$.²⁰ This result supports the finding that the surface of the nanosheets is the {0001} planes of the hexagonal $\beta\text{-Ni}(\text{OH})_2$ phase. Elemental mapping of the $\text{TiO}_2@/\text{Ni}(\text{OH})_2$ composite in Fig. 2i shows the distribution of elements in the hierarchical hollow nanostructure. The weaker contrast in the core of the structure and the absence of the element Si confirm that the core of the sphere is hollow with the successful removal of the SiO_2 spheres by the OH^- ions in the growth solution. The TiO_2 shell is well-formed and there is a uniform distribution of $\text{Ni}(\text{OH})_2$ nanosheets on the surface of the hollow sphere. The XRD patterns of the nanostructures at various stages of their formation are shown in Fig. 2j. No peak was observed in the diffraction pattern of the SiO_2 spheres because of its amorphous nature. Upon the growth of TiO_2 shells on the SiO_2 spheres, several peaks

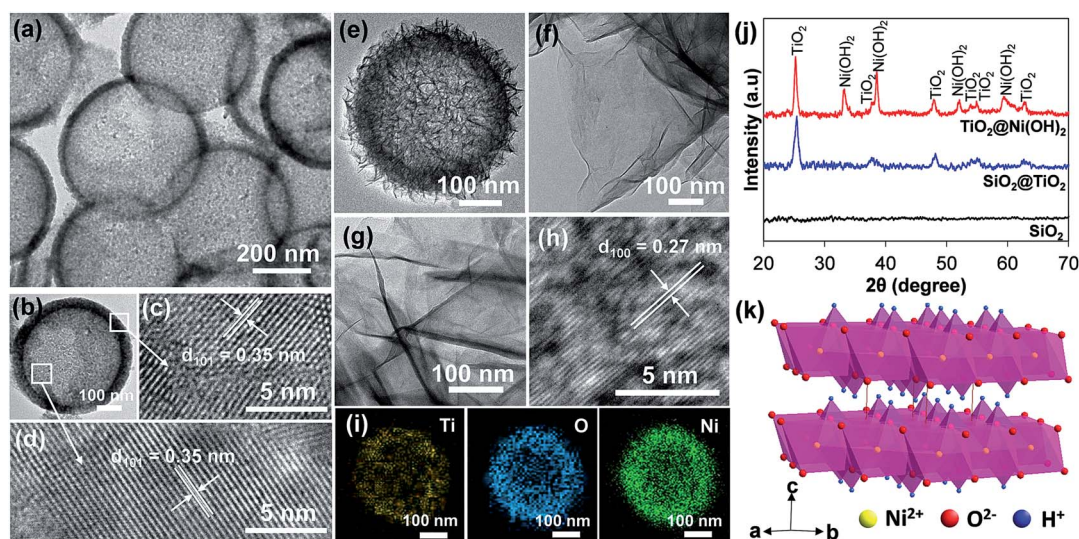


Fig. 2 (a and b) Low resolution TEM images of hollow TiO_2 nanospheres. (c and d) HRTEM of marked regions on the TiO_2 shell of the hollow core structure. (e) TEM of $\text{TiO}_2@/\text{Ni}(\text{OH})_2$ hierarchical hollow spheres. (f and g) TEM images of expansive and thin planar 2D $\text{Ni}(\text{OH})_2$ nanosheets. (h) HRTEM of $\text{Ni}(\text{OH})_2$ nanosheets. (i) Elemental mapping of $\text{TiO}_2@/\text{Ni}(\text{OH})_2$ hierarchical hollow spheres. (j) XRD pattern of the various composites. (k) Crystal structure of $\text{Ni}(\text{OH})_2$.

observed at 25.34, 37.91, 48.10, 54.14, 55.17 and 62.73° could be indexed to the (101), (004), (200), (105), (211) and (204) crystal planes of the anatase phase of TiO₂ (JCPDS card no. 21-1272). After the Ni(OH)₂ nanosheets were grown on the SiO₂@TiO₂ spheres with an *in situ* etching of the SiO₂ core, peaks from both β-Ni(OH)₂ and anatase phase of TiO₂ were observed. This suggests that Ni(OH)₂ sheets were successfully grown without altering the phase of the TiO₂ shell. The diffraction peaks at 33.08, 38.51, 52.18, and 59.56° were indexed to (100), (101), (102) and (110) planes of the pure hexagonal phase of β-Ni(OH)₂ (JCPDS card no. 14-0117). To determine the presence of the various elements and their chemical states, XPS analysis was performed and the spectra are shown in Fig. S2.† The Ni 2p_{3/2} and 2p_{1/2} peaks obtained were located at 855.6 eV and 873.2 eV respectively, together with two shake-up satellite peaks, indicating that Ni exists as Ni(OH)₂.²¹ The spin-energy separation of 17.6 eV is also representative of the Ni(OH)₂ phase.²² The Ti 2p_{3/2} and 2p_{1/2} peaks observed at 458.8 eV and 464.4 eV respectively indicate that Ti is present as Ti⁴⁺ in the form of TiO₂.²³ The O 1s peak can be deconvoluted into three peaks at 529.9 eV, 530.4 eV and 532 eV. The O 1s peak located at 529.9 eV is attributed to the Ti–O–Ti bond, confirming the presence of TiO₂.²³ The peak at 530.4 eV is associated with Ni(OH)₂, while the peak at 532 eV can be assigned to the chemisorbed hydroxyl group.¹⁹ These results correspond with the XRD analysis results, confirming the presence of Ni(OH)₂ and TiO₂. At this point, it is apparent that the crystalline hexagonal layered structure, β-Ni(OH)₂ with an intrinsic lamellar structure as depicted in Fig. 2k, has been prepared. The 2D layered structure, which is largely made up of exposed surfaces, can enable intimate and large area contact and hence is expected to improve interfacial charge transfer for highly surface-dependent electro/photocatalytic redox reactions.

The samples were also characterized by cyclic voltammetry (CV) in 1 M NaOH electrolyte. No redox peaks were observed in

the CV curve for TiO₂ spheres due to the absence of redox reactions. The CV curves of TiO₂@Ni(OH)₂ in the potential window of 0 to 0.6 V (*vs.* SCE) at various scan rates are shown in Fig. 3a. An anodic oxidation peak at 0.46 V and correspondingly an oxyhydroxide reduction peak at 0.28 V were determined at 1 mV s⁻¹. The current responses increase accordingly with the scan rates, while retaining the shapes of the CV curves, which suggests that the porous core-shell structure and its 2D hydrated layered Ni(OH)₂ nanosheets are beneficial for fast redox reactions. During the cathodic scan, the reduction of Ni³⁺ to Ni²⁺ leads to bleaching of the film. In the reverse anodic scan, the oxidation of Ni²⁺ to Ni³⁺ causes coloration of the film.^{24,25} The OH⁻ intercalation–deintercalation and electron transfer can be attributed to the electrochemical reactions of Ni(OH)₂ as follows:^{26,27}



The switching speed between the bleached and colored states is one of the important factors in consideration for electrochromic applications.²⁸ The changes in transmittance were tested at different bias voltages of 1.0, 1.5 and 2.0 V to investigate the effects on the response time and maximum optical contrast attainable. From the plots shown in Fig. 3b, the difference in the transmittance contrasts between the bleached and colored states reduces as the bias voltage decreases. This stems from the reduction of driving force for the transport of the charges, hence leading to a slower conversion rate of Ni(OH)₂ to NiOOH and *vice versa*. Upon closer inspection of the ±2 V cycle, it is noted that it takes about 4.2 and 0.6 s to attain 90% change in bleaching and coloration transmittance of the TiO₂@Ni(OH)₂ coating respectively. The fast switching speed of TiO₂@Ni(OH)₂ can be attributed to the porous core-shell

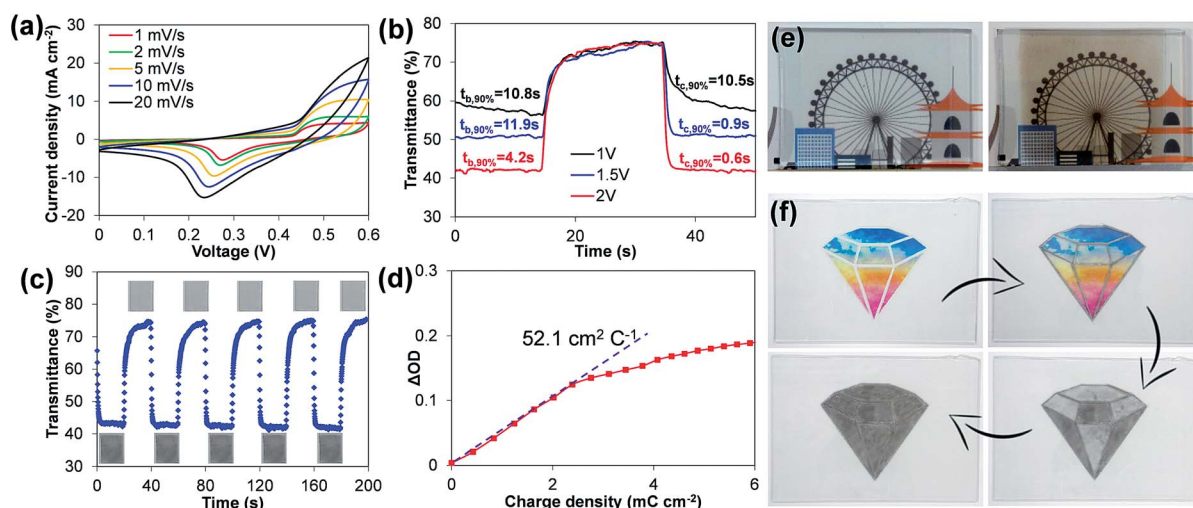


Fig. 3 (a) Cyclic voltammograms of TiO₂@Ni(OH)₂ in 1 M NaOH at various scan rates. (b) Transmittance spectra of coated glass in one cycle of bleaching and coloration at various voltage biases. (c) Transmittance spectra of coated glass over five consecutive cycles of bleaching and coloration with ±2 V bias. (d) Optical density vs. charge density of TiO₂@Ni(OH)₂ coated glass recorded at 550 nm. (e) Optical photographs of coated glass in bleached (left) and colored (right) states. (f) Optical photographs of an actively controllable electrochromic display with a crystal design.

structure and its 2D hydrated layered $\text{Ni}(\text{OH})_2$ nanosheets of large surface area and reduced diffusion path lengths that effectively facilitate the intercalation/deintercalation of ions. The repeatability of the electrochromic effect is shown in Fig. 3c where the voltage bias was switched between +2 V and -2 V repeatedly and the corresponding change in transmittance over time was measured. Each bias state was maintained for 20 s before switching to the opposite polarity. It can be seen that over the 5 switching cycles, the $\text{TiO}_2@\text{Ni}(\text{OH})_2$ coated FTO glass consistently exhibited a transmittance level of 75% in the bleached state and 41% in its colored state. Digital micrographs of reversible bleached and colored states of the $\text{TiO}_2@\text{Ni}(\text{OH})_2$ coating are shown in Fig. 3c insets. This shows that the electrochromic effect of $\text{TiO}_2@\text{Ni}(\text{OH})_2$ is stable over the optical modulation cycles possibly owing to the porous and void spaces of the core-shell configuration that can accommodate volumetric changes without undergoing cycling structural alteration/degradation.

Coloration efficiency (CE) denotes the extent of optical modulation with the supplied unit charge per area.

$$\text{CE}(\lambda) = \frac{\Delta\text{OD}(\lambda)}{Q} \quad (2)$$

$$\Delta\text{OD}(\lambda) = \log \frac{T_b}{T_c} \quad (3)$$

where ΔOD is the change in optical density at a specific wavelength, Q is the total electronic charge density, T_c and T_b are the transmittances of the colored and bleached states respectively. Fig. 3d shows the plot of ΔOD versus Q measured at $\lambda = 550$ nm, where CE was determined from the slope of the fitted linear region. A CE of $52.1 \text{ cm}^2 \text{ C}^{-1}$ is attained from the $\text{TiO}_2@\text{Ni}(\text{OH})_2$ nanocomposite which is higher than the reported CE of $\text{Ni}(\text{OH})_2$ and NiO in several papers.^{29–32} A higher CE indicates a more ready color change of an electrochromic film with a smaller charge density input. It is evident that in the bleached state, a high level of transparency of the coating can be obtained since the colored background is clearly visible through the coated glass (Fig. 3e). At 2 V bias, the coated FTO glass switched to the colored state of a brownish hue which is a characteristic of electrochromogenic $\text{Ni}(\text{OH})_2$ (Fig. 3e). Furthermore, the selectivity and extent of contrast can be radically tuned to show the

promises of an actively controllable electrochromic display (Fig. 3f). The display evolves from a clear coated glass that allows high transmittance of a colorful crystal backdrop to selective dark brown outline/framework coloration. Next, a voltage bias of 1 V (lighter coloration) or 2 V (darker coloration) was applied to selective individual patterned segments of the crystal to attain a display with alternating contrasts. A subsequent 2 V bias was applied to reconfigure the display, producing a uniform dark coloration across all segments. This validates an active transmittance modulated coating upon application of modest input voltage, hence making it an ideal inexpensive dynamic display.

Besides electrochromism, the $\text{TiO}_2@\text{Ni}(\text{OH})_2$ composite also possesses heat shielding and VOC degradation functionalities as summarized in Fig. 4a which illustrates the concept of a multi-functional all-in-one window.^{33,34} The transmittance spectra in Fig. 4b show the transmittance of uncoated glass, and the $\text{TiO}_2@\text{Ni}(\text{OH})_2$ composite coated glass in both the bleached and colored states across a wide spectrum of wavelength. The reference air mass (AM) 1.5 spectrum which represents the solar radiation is shown in the background of the graph. The AM 1.5 spectrum has been purposefully color coded to define the UV, visible and near-infrared (NIR) segments of solar irradiation. As shown in Fig. 4b, an uncoated glass substrate actually transmits close to 90% of the emission from the sun across the entire spectrum. However, upon coating the $\text{TiO}_2@\text{Ni}(\text{OH})_2$ composite, the bleached coated glass shows a remarkable decrease in transmission across all wavelengths, with the visible light region still having a transmittance level of about 75–80%. This means that the $\text{TiO}_2@\text{Ni}(\text{OH})_2$ coating is capable of decreasing the transmittance of both harmful UV rays and also heat-generating NIR irradiation to 40–50%, but allows most of the visible light to pass through. This is essential for electrochromic windows which are expected to reduce the amount of UV and NIR rays passing through the window but still allow the occupants to see the view outside. Upon coloration of the $\text{TiO}_2@\text{Ni}(\text{OH})_2$ coating with the application of a 2 V voltage bias, there was further reduction in transmission across all wavelengths, with the transmittance in the visible wavelengths dropping to about 40%. The transmittance spectra of the colored $\text{TiO}_2@\text{Ni}(\text{OH})_2$ coating at various applied biases is shown in Fig. S3.† This allows the colored coating on a glass

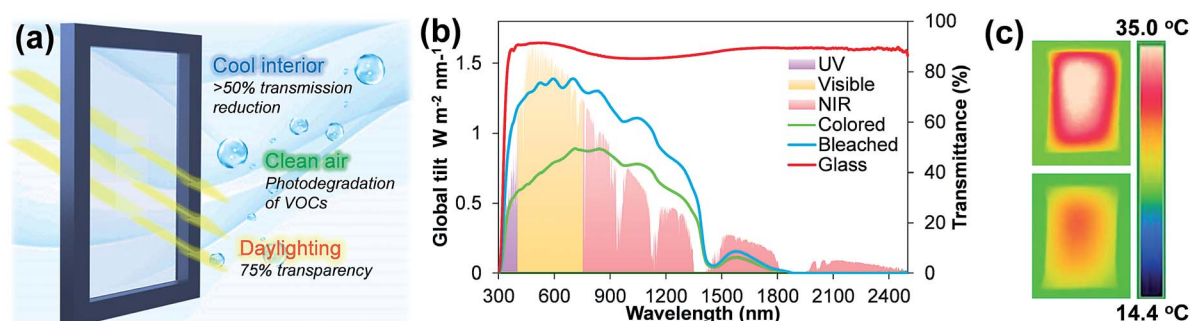


Fig. 4 (a) Illustration of the multi-functional all-in-one window concept. (b) Transmittance spectra of uncoated and $\text{TiO}_2@\text{Ni}(\text{OH})_2$ coated glass with AM 1.5 reference spectrum. (c) Thermal imaging of Armaflex® foam heated up with a Xe arc lamp.

window to reduce the glare from the sunlight and also keep the room cool by blocking out the NIR irradiation. This heat blocking property is shown by the thermal images in Fig. 4c. In this experiment, a piece of glass was placed between a Xe arc lamp and a piece of Armaflex® foam. When an uncoated piece of glass was used, most of the NIR radiation from the Xe lamp could pass through the glass and heat up the foam to about 35 °C (top of Fig. 4c). When a $\text{TiO}_2@\text{Ni}(\text{OH})_2$ coated glass was used, a substantial amount of NIR radiation was blocked out resulting in the foam being heated up to only 29 °C (bottom of Fig. 4c). This difference in temperature proves that the $\text{TiO}_2@\text{Ni}(\text{OH})_2$ composite is able to effectively reduce the transmission of NIR radiation.

The stability of the electrochromic property of $\text{TiO}_2@\text{Ni}(\text{OH})_2$ is shown in Fig. 5a, where the coated glass was repeatedly switched between the bleached and colored states at different voltage biases. The transmittances of the coating in the bleached and colored states were observed to be consistent. The electrochromic cycling stability test on the sample was then extended to 5000 cycles at ± 2 V and the plot is shown in Fig. S4.† The transmittance levels in both the bleached (75%) and colored (41%) states were relatively stable up to 4000 cycles, after which the transmittance dropped by 15% and 4% for the bleached and colored states respectively at the end of 5000 cycles. This degradation in performance is most likely attributed to $\text{Ni}(\text{OH})_2$, and this has been reported and discussed by Ren *et al.*³⁵ and Liu *et al.*³⁶ During coloration potential cycling of $\text{Ni}(\text{OH})_2$ in an alkali electrolyte, NiOOH structures are formed

together with intercalated water molecules. Over time, the increasing intercalation of water will surround and isolate the regions of NiOOH during the coloration process. It is postulated that this isolation will impede the diffusion of OH^- ions from NiOOH to the cathode, thus preventing the isolated NiOOH from being bleached. As the network of water intercalation during coloration extends with further cycling, more and more areas of NiOOH will be isolated and remain colored even during the bleaching cycle. It is also possible to color or bleach specific regions of the coated glass with the application of the voltage bias to selective regions as shown in Fig. 5b. The first photo of Fig. 5b shows a prototype made of $\text{TiO}_2@\text{Ni}(\text{OH})_2$ coated polyethylene terephthalate (PET), demonstrating the possibility of fabricating a flexible electrochromic device. The second photo in Fig. 5b shows a picture of a yellow triangle with laboratory-related symbols clearly visible through the bleached coated glass indicating the high transparency of the coating. The subsequent photos show that selective regions of the coating can be colored or bleached, demonstrating controllability over the electrochromic effect. The VOC degradation performance of the $\text{TiO}_2@\text{Ni}(\text{OH})_2$ composite was investigated and compared with that of $\text{SiO}_2@\text{TiO}_2$ spheres and hollow TiO_2 spheres for methanol and formaldehyde (Fig. 5c). $\text{TiO}_2@\text{Ni}(\text{OH})_2$ performed the best while the $\text{SiO}_2@\text{TiO}_2$ spheres consistently performed the worst in both types of VOCs. The poor performance of the $\text{SiO}_2@\text{TiO}_2$ spheres can be attributed mainly to their low surface area, which results in fewer reactive sites available for degradation of the VOC molecules, and also the

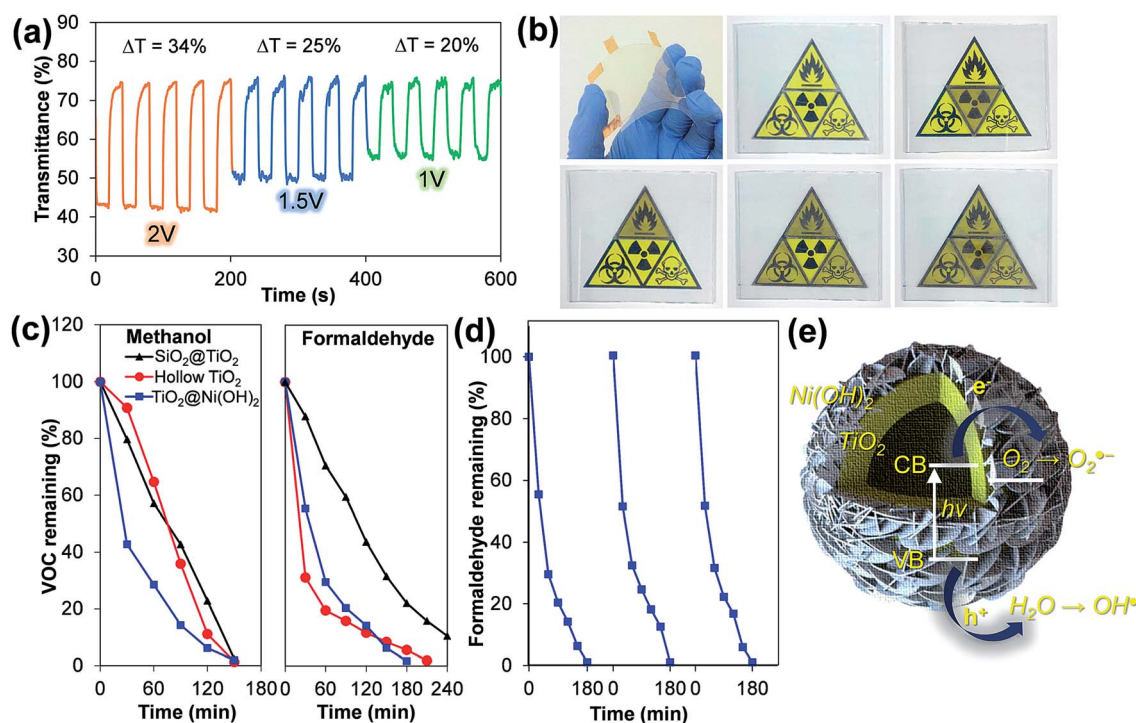
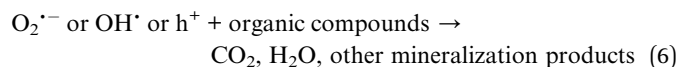


Fig. 5 (a) Transmittance spectra of $\text{TiO}_2@\text{Ni}(\text{OH})_2$ coated glass over consecutive cycles of bleaching and coloration with various voltage biases. (b) Photos showing a flexible electrochromic device and selective coloration and bleaching. (c) Photocatalytic degradation of methanol and formaldehyde. (d) Repeated cycling of photocatalytic degradation of formaldehyde. (e) Schematic diagram showing the charge transfer mechanism between $\text{Ni}(\text{OH})_2$ and TiO_2 .

rapid recombination of the photogenerated electrons and holes. The enhancement in VOC degradation exhibited by the hollow TiO₂ spheres and the TiO₂@Ni(OH)₂ hierarchical hollow spheres can be attributed to 2 factors, namely the hollowing out of the TiO₂ spheres and the reduction in charge recombination due to the presence of Ni(OH)₂. The hollow structure of the composite results in a higher surface area and also an enhancement in light absorption due to multiple-scattering within the hollow cavity of the spheres as shown in Fig. 1i. The TiO₂@Ni(OH)₂ composite can be used repeatedly for the degradation of VOCs as shown in Fig. 5d, where the sample was tested for repeated degradation of formaldehyde. The degradation performance was consistent throughout the 3 cycles and formaldehyde could be fully degraded in 180 min in all 3 cycles, demonstrating the stability of the composite as a photocatalyst for VOC degradation. The co-catalytic effect of Ni(OH)₂ on TiO₂ is shown by the schematic diagram in Fig. 5e which illustrates the alignment of the conduction and valence bands of TiO₂ in relation to Ni(OH)₂. When the composite is illuminated, the photogenerated electrons will be preferentially transferred to Ni(OH)₂,³⁷ hence reducing recombination of the photogenerated charge carriers. The transferred electrons then reduce the adsorbed oxygen to oxygen peroxide radicals (O₂^{•-}) as shown in eqn (4).



The positively charged holes (h⁺) react with adsorbed water to form hydroxyl radicals (OH[•]) (eqn (5)).^{38,39} O₂^{•-} and OH[•] radicals are powerful oxidizing agents capable of degrading organic compounds into CO₂, H₂O and other mineralization products (eqn (6)). The organic compounds can also be oxidized by holes.^{40,41}



Conclusions

We have successfully synthesized hollow TiO₂ nanospheres decorated with 2D hydrated layered Ni(OH)₂ nanosheets with complementary electrochromic and photocatalytic degradation properties. The composite material has a coloration efficiency of 52.1 cm² C⁻¹ and fast switching speeds between the bleached and colored states. It is also possible to actively tune the optical transmittance of selected regions of the TiO₂@Ni(OH)₂ coated glass. On top of electrochromism, the composite layer is able to block out UV and NIR radiation which is essential for potential adoption in electrochromic windows. The composite material also exhibited enhanced photocatalytic degradation of VOCs with consistent performance over several cycles due to the co-catalytic effect of Ni(OH)₂ nanosheets when coupled with hollow TiO₂ nanospheres. This monolithically integrated multiple functionalities material system provides a solution to

photocatalytic environmental and chromogenic energy conservation issues that may emerge in future building requirements.

Acknowledgements

This research is supported by the National Research Foundation (NRF), under Energy Innovation Research Programme (EIRP) R-263-000-B82-279, managed on behalf of Building and Construction Authority (BCA).

References

- 1 S. Guo and S. Dong, *Chem. Soc. Rev.*, 2011, **40**, 2644.
- 2 V. Rives and M. a. Angeles Ulibarri, *Coord. Chem. Rev.*, 1999, **181**, 61.
- 3 Q. Wang and D. O'Hare, *Chem. Rev.*, 2012, **112**, 4124.
- 4 T. Heine, *Acc. Chem. Res.*, 2015, **48**, 65.
- 5 M. Osada and T. Sasaki, *J. Mater. Chem.*, 2009, **19**, 2503.
- 6 C. Tan and H. Zhang, *Nat. Commun.*, 2015, **6**, 7873.
- 7 J. Guo, B. Jiang, X. Zhang, L. Tang and Y.-h. Wen, *J. Mater. Chem. A*, 2015, **3**, 2251.
- 8 B. Li, M. Ai and Z. Xu, *Chem. Commun.*, 2010, **46**, 6267.
- 9 M. L. Carl, in *Large Area Chromogenics: Materials and Devices for Transmittance Control*, 1989.
- 10 K. S. Novoselov, A. K. Geim, S. V. Morozov, D. Jiang, Y. Zhang, S. V. Dubonos, I. V. Grigorieva and A. A. Firsov, *Science*, 2004, **306**, 666.
- 11 V. Nicolosi, M. Chhowalla, M. G. Kanatzidis, M. S. Strano and J. N. Coleman, *Science*, 2013, 340.
- 12 Q. Ji, Y. Zhang, Y. Zhang and Z. Liu, *Chem. Soc. Rev.*, 2015, **44**, 2587.
- 13 L. Song, L. Ci, H. Lu, P. B. Sorokin, C. Jin, J. Ni, A. G. Kvashnin, D. G. Kvashnin, J. Lou, B. I. Yakobson and P. M. Ajayan, *Nano Lett.*, 2010, **10**, 3209.
- 14 W. Stöber, A. Fink and E. Bohn, *J. Colloid Interface Sci.*, 1968, **26**, 62.
- 15 S. Son, S. H. Hwang, C. Kim, J. Y. Yun and J. Jang, *ACS Appl. Mater. Interfaces*, 2013, **5**, 4815.
- 16 C. F. Bohren and D. R. Huffman, in *Absorption and Scattering of Light by Small Particles*, Wiley-VCH Verlag GmbH, 2007, ch. 4, p. 82, DOI: 10.1002/9783527618156.
- 17 Z. Han, F. Tongxiang, H. Ting, L. Xufan, D. Jian, Z. Di, G. Qixin and O. Hiroshi, *Nanotechnology*, 2009, **20**, 085603.
- 18 M. Wan, W. Li, Y. Long and Y. Tu, *Anal. Methods*, 2012, **4**, 2860.
- 19 Z. Xu, J. Yu, G. Liu, B. Cheng, P. Zhou and X. Li, *Dalton Trans.*, 2013, **42**, 10190.
- 20 X. Xia, J. Luo, Z. Zeng, C. Guan, Y. Zhang, J. Tu, H. Zhang and H. J. Fan, *Sci. Rep.*, 2012, **2**, 981.
- 21 S. Xie, T. Zhai, W. Li, M. Yu, C. Liang, J. Gan, X. Lu and Y. Tong, *Green Chem.*, 2013, **15**, 2434.
- 22 J. Yan, Z. Fan, W. Sun, G. Ning, T. Wei, Q. Zhang, R. Zhang, L. Zhi and F. Wei, *Adv. Funct. Mater.*, 2012, **22**, 2632.
- 23 W. L. Ong, Y.-F. Lim, J. L. Ting Ong and G. W. Ho, *J. Mater. Chem. A*, 2015, **3**, 6509.
- 24 G. A. Niklasson and C. G. Granqvist, *J. Mater. Chem.*, 2007, **17**, 127.

- 25 C. G. Granqvist, *Thin Solid Films*, 2014, **564**, 1.
- 26 Y. Takahashi and T. Tatsuma, *Langmuir*, 2005, **21**, 12357.
- 27 J. S. E. M. Svensson and C. G. Granqvist, *Appl. Phys. Lett.*, 1986, **49**, 1566.
- 28 S.-Y. Kao, Y. Kawahara, S. i. Nakatsuji and K.-C. Ho, *J. Mater. Chem. C*, 2015, **3**, 3266.
- 29 X. H. Xia, J. P. Tu, J. Zhang, X. L. Wang, W. K. Zhang and H. Huang, *Sol. Energy Mater. Sol. Cells*, 2008, **92**, 628.
- 30 R. A. Patil, R. S. Devan, J.-H. Lin, Y.-R. Ma, P. S. Patil and Y. Liou, *Sol. Energy Mater. Sol. Cells*, 2013, **112**, 91.
- 31 M. R. J. Scherer and U. Steiner, *Nano Lett.*, 2013, **13**, 3005.
- 32 S.-H. Lin, F.-R. Chen and J.-J. Kai, *Appl. Surf. Sci.*, 2008, **254**, 3357.
- 33 C.-H. Wu, C.-Y. Hsu, K.-C. Huang, P.-C. Nien, J.-T. s. Lin and K.-C. Ho, *Sol. Energy Mater. Sol. Cells*, 2012, **99**, 148.
- 34 L.-M. Huang, C.-W. Hu, H.-C. Liu, C.-Y. Hsu, C.-H. Chen and K.-C. Ho, *Sol. Energy Mater. Sol. Cells*, 2012, **99**, 154.
- 35 Y. Ren, W. K. Chim, L. Guo, H. Tanoto, J. Pan and S. Y. Chiam, *Sol. Energy Mater. Sol. Cells*, 2013, **116**, 83.
- 36 J. Liu, Y. Ren, B. Dasgupta, H. Tanoto, H. L. Seng, W. K. Chim, S. F. Y. Li and S. Y. Chiam, *J. Mater. Chem. A*, 2013, **1**, 15095.
- 37 J. Yu, Y. Hai and B. Cheng, *J. Phys. Chem. C*, 2011, **115**, 4953.
- 38 D. F. Ollis, E. Pelizzetti and N. Serpone, *Environ. Sci. Technol.*, 1991, **25**, 1522.
- 39 M. Anpo, T. Shima and Y. Kubokawa, *Chem. Lett.*, 1985, **14**, 1799.
- 40 O. Micic, Y. Zhang, K. R. Cromack, A. Trifunac and M. Thurnauer, *J. Phys. Chem.*, 1993, **97**, 13284.
- 41 W. H. Glaze, J. F. Kenneke and J. L. Ferry, *Environ. Sci. Technol.*, 1993, **27**, 177.